Symmetry-resolved electronic band structure of quasi-one-dimensional $HfSe_3$(001)

Gauthami Viswan,[1] Bushra Ashraf,[2] Jose Avila,[3] Duy Le,[2] Alexey Lipatov,[4,5] Takashi Komesu,[1] Alexander Sinitskii,[4] Talat S. Rahman,[2] Maria C. Asensio,[6,7] and Peter A. Dowben[1]

[1]*Department of Physics and Astronomy, University of Nebraska-Lincoln, Lincoln, Nebraska 68588-0299, USA*
[2]*Department of Physics, University of Central Florida, Orlando, Florida 32816, USA*
[3]*Synchrotron SOLEIL and Universite Paris-Saclay, L'Orme des Merisiers, BP48, 91190 Saint-Aubin, France*
[4]*Department of Chemistry, University of Nebraska-Lincoln, Lincoln, Nebraska 68588-0304, USA*
[5]*Department of Chemistry, Biology and Health Sciences, South Dakota School of Mines and Technology, Rapid City, South Dakota 57701, USA*
[6]*Madrid Institute of Materials Science (ICMM), Spanish Scientific Research Council (CSIC), Cantoblanco, E-28049 Madrid, Spain*
[7]*MATINÉE: CSIC Associated Unit Between the Institute of Materials Science at the University of Valencia (ICMUV) and ICMM, Cantoblanco, 28049 Madrid, Spain*

(Received 27 October 2025; revised 12 December 2025; accepted 6 January 2026; published 2 February 2026)

In this work, the band structure of quasi-one-dimensional $HfSe_3$ was investigated with nanospot angle-resolved photoemission spectroscopy (nano-ARPES) in both the *p*- and *s*-polarization geometries and with density functional theory calculations. $HfSe_3$ has a rectangular surface Brillouin zone where the effective hole mass along the chain direction ($\bar{\Gamma}$ to $\bar{Y}$) measured with *p*-polarization geometry is $-0.27 \pm 0.01\ m_e$, which is smaller than the effective hole mass along the direction perpendicular to the chains measured with *s*-polarization geometry ($\bar{\Gamma}$ to $\bar{B}$), $-1.17 \pm 0.01\ m_e$, in agreement with the calculated hole masses of $-0.25\ m_e$ ($\bar{\Gamma}$ to $\bar{Y}$) and $-1.11\ m_e$ ($\bar{\Gamma}$ to $\bar{B}$), respectively. A band separation of 0.22 ± 0.01 eV is observed at the top of the valence band in the experimental band structure along $\bar{\Gamma}$ to $\bar{Y}$. This band separation may be partly enhanced due to intrinsic spin-orbit coupling effects, as the band structure calculated with density functional theory shows a significant separation of 0.29 eV, for the two bands closest to the top of the valence band along $\bar{\Gamma}$ to $\bar{Y}$, only when spin-orbit interactions are included.

DOI: 10.1103/k4sz-qkh6

I. INTRODUCTION

It is widely acknowledged that the layered transition-metal trichalcogenide (TMTC) semiconductors, such as TiS_3 [1–13], $TiSe_3$ [7], ZrS_3 [3,4,7,10,14–17], $ZrSe_3$ [7,14,16,18–20], HfS_3 [10,14,21], and $HfSe_3$ [14,18], have highly anisotropic band structures. These quasi-one-dimensional (1D) materials give rise to highly anisotropic optical properties [4,18,20–36] and dichroitic phototransistors have been demonstrated [4,19,21,22,24,25,35]. There is, furthermore, a loss of inversion symmetry at the surface, and indeed, there are no mirror planes at the (001) surface, permitting the demonstration of a chiral phototransistor for TiS_3(001) [37]. Yet, in spite of the loss of crystalline symmetry at the metal trichalcogenide MX_3(001) surface (M = Ti, Zr, Hf; X = S, Se), band symmetries are still generally preserved [4].

It has been suggested that the band separation at the top of the valence band for ZrS_3 and especially for $ZrSe_3$ and $HfSe_3$ is the result of spin-orbit coupling effects [18]. If true, this makes two-dimensional (2D) layers of the TMTCs with higher atomic number (Z) possible candidates for spintronic transistor devices due to the enhancement in on/off ratio [38–40]. Indeed, this would be spintronics without magnetism [38–40] because of the enhanced spin-orbit coupling.

As band symmetries were not assigned in the prior work [18], it is paramount to investigate the electronic structure of $HfSe_3$ in depth to determine whether the band symmetries are preserved, as have been observed for TiS_3(001) [4], MoS_2(0001) [41], and WSe_2(0001) [42], even in the absence of any mirror plane. Few such experimental studies exist for the trichalcogenides, and this is a deficiency because the transition-metal trichalcogenides belong to a small group of materials for which the calculational methodology can result in surprisingly large variations in the band structure. These variations in theory are evident in the wide range of calculated hole effective mass by as much as 20% for TiS_3 (on comparing [8] to [6]), more than 100% for ZrS_3 (from comparing [17] to [15]) and $ZrSe_3$ (comparing [14] to [7]), and sometimes theory even fails to correctly predict whether the light hole mass is along or perpendicular to the quasi-one-dimensional TMTC chains (as in the theory for ZrS_3 [7,10,14–17] vs the experimental band structure [3]).

The goal of the present work is to investigate the electronic structure of the quasi-1D $HfSe_3$(001) in great depth to explore the role of band symmetry, spin-orbit coupling, and anisotropy in the hole effective mass. This effort compares the experimental band structure of $HfSe_3$, obtained from nanospot angle-resolved photoelectron spectroscopy (nano-ARPES) in both the *p*- and *s*-polarization geometries, with the theoretical band structure obtained from density-functional-theory (DFT) calculations, as has been done successfully for MoS_2(0001) [41] and WSe_2(0001) [42].

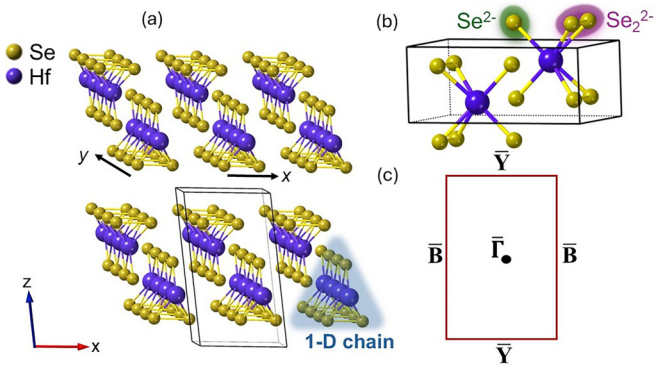

FIG. 1. (a) The schematic of layered quasi-one-dimensional (1D) chains of $HfSe_3$ with the crystallographic $\vec{\mathbf{b}}$ axis direction specified. (b) The unit cell of $HfSe_3$ highlights the inner selenide (Se^{2-}) and outer diselenide (Se_2^{2-}) species. (c) The surface Brillouin zone of $HfSe_3(001)$ with the nominal high-symmetry points labeled.

II. METHODOLOGIES

The $HfSe_3$ crystals were synthesized by chemical vapor transport of metallic hafnium foil and selenium powder in a quartz ampule sealed under vacuum of about 200 mTorr at 600 °C, as described in the Supplemental Material in more detail [43]. The long black nanowhiskers of $HfSe_3$ (Supplemental Material Fig. S1 [43]) were characterized by powder X-ray diffraction (XRD) measurements at room temperature. The XRD spectrum of $HfSe_3$ (Supplemental Material Fig. S2 [43]) indicates a primitive monoclinic structure with space group $P2_1/m$ and lattice constants $a = 5.379$ Å, $b = 3.716$ Å, $c = 9.412$ Å, and the cant angle of $\beta = 97.585°$. These values remain within the range of previously reported values [16,44]. The crystallographic $\vec{b}$ axis of $HfSe_3$ crystals, which we assign as the y axis, is along the chains as shown in Fig. 1(a). Like the other metal trichalcogenide isostructural counterparts, such as HfS_3 [21], $HfSe_3$ has two distinct species of a chalcogen atom, in this case Se atoms, where the inner Se atoms are selenide (Se^{2-}) and the outer ones are diselenide (Se_2^{2-}), as can be seen in Fig. 1(b). It is also worth noting that the rows of inner Se atoms align with $\vec{b}$, and the diselenide bridges of outer Se atoms are perpendicular to the chain direction.

The occupied band structure of $HfSe_3$ crystals along both $\bar{\Gamma}$ to $\bar{Y}$ and $\bar{\Gamma}$ to $\bar{B}$ high-symmetry directions are studied using nano-ARPES done at the ANTARES beamline at the SOLEIL synchrotron [45]. The nanowhiskers of $HfSe_3$ were exfoliated *in situ* under ultrahigh vacuum. The spectroscopic imaging mode of the ANTARES microscope in the analysis chamber at the experimental end station was used to ensure the precise alignment of the $HfSe_3$ crystals along the high-symmetry directions of the Brillouin zone to the correct beamline geometry using the nanospot x-ray illumination with spot size of ∼500 nm [2–4,45,46]. The high-resolution MBS A-1 hemispherical electron analyzer allowed the detection of photoelectrons with an energy resolution better than ∼40 meV at room temperature and angular resolution of ∼0.2°.

The nanospot size of the incident photon flux ensured that the incident radiation was focused on a single individual nanowhisker during the angle-resolved spectroscopic measurements. According to the crystallographic coordinate system of $HfSe_3(001)$, the surface Brillouin zone is rectangular, as shown in Fig. 1(c). The key reciprocal space directions from the Brillouin zone center ($\bar{\Gamma}$) are $\bar{\Gamma}$ to $\bar{Y}$, which corresponds to wave vectors along 1D chains of $HfSe_3$ in real space, while $\bar{\Gamma}$ to $\bar{B}$ is the surface Brillouin zone direction perpendicular to the 1D chains of $HfSe_3$. Based on the lattice constants a and b obtained from XRD (Supplemental Material Fig. S2 [43]), in reciprocal lattice space, the distance from $\bar{\Gamma}$ to $\bar{B}$ is 0.584 $Å^{-1}$ and from $\bar{\Gamma}$ to $\bar{Y}$ is 0.845 $Å^{-1}$. To investigate the two different nominally high symmetry directions along the surface Brillouin zone of the $HfSe_3$ nanorods, we used two different alignments of the analyzer slit with respect to the $HfSe_3(001)$ chains. The band dispersions along the $\bar{\Gamma}$ to $\bar{Y}$ and $\bar{\Gamma}$ to $\bar{B}$ directions were obtained by aligning the analyzer slit parallel and perpendicular to the 1D chains, respectively. For the purposes of this work, the band symmetries assignments use the coordinate system of $\langle z \rangle$ to be along the surface normal, $\langle y \rangle$ to be along the chains, in the plane of the surface (or $\bar{\Gamma}$ to $\bar{Y}$ in reciprocal space), while the $\langle x \rangle$ is to be perpendicular to the chains, in the plane of the surface (or $\bar{\Gamma}$ to $\bar{B}$ in reciprocal space), consistent with the conventions of most surface science studies.

The experimental band structure was acquired in two different photoemission geometries, *p*-polarization (even symmetry) and *s*-polarization (odd symmetry), where the incident light vector potential ($\vec{A}$) is along the scan plane and perpendicular to the scan plane, respectively. The use of the two different photoemission geometries allows us to characterize the even and odd initial valence-band states along different high-symmetry directions. Throughout this work we have used vertically polarized light and have obtained two orientations, one case in which the incident light polarization is parallel to the 1D chains and a second case in which the sample is rotated in such a way that the incident light polarization is perpendicular to the 1D chains.

The orbital-resolved electronic band structure of $HfSe_3$ was calculated using DFT as implemented in the QUANTUM ESPRESSO package [47]. To balance computational feasibility with accuracy, calculations were carried out using two sets of exchange correlation functionals. For geometric structure minimization (ionic relaxation) the exchange-correlation energy was treated within the generalized gradient approximation (GGA) [48] using the Perdew–Burke–Ernzerhof (PBE) functional [49]. Van der Waals interactions were included using Grimme's DFT-D3 correction [50]. All calculations employed optimized norm-conserving Vanderbilt (ONCV) pseudopotentials [51] in both scalar-relativistic and fully relativistic forms for calculations without and with the inclusion of spin-orbit coupling (SOC) interactions, respectively. The electronic wave functions were expanded in a plane-wave basis set with a kinetic energy cutoff of 60 Ry. Self-consistent calculations were converged to 10^{-6} Ry, and atomic positions were relaxed until all forces were smaller than 0.001 Ry/Bohr. Our simulation supercell, based on one-layer $HfSe_3$, was constructed with the optimized lattice constant of $a = 5.35$ Å, $b = 3.71$ Å. A vacuum spacing of 22 Å was introduced,

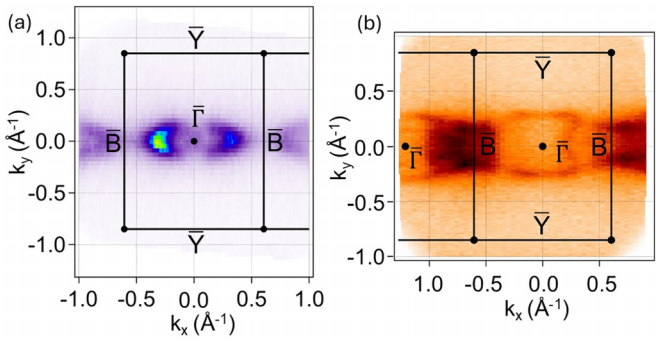

FIG. 2. The isoenergy (constant energy) contour plots taken using an incident photon energy of 95 eV with two different sample orientations, (a) where the incident light is along the chains and (b) where the incident light is perpendicular to the chain direction, taken at binding energies 0.3 eV and 0.5 eV below the top of the valence band, respectively, or 0.7 eV and 0.9 eV below the Fermi level, respectively. The edges of the surface Brillouin zone indicated by black bold lines show the difference in high-symmetry directions based on the sample orientation.

between layers, to avoid spurious interactions between periodic images. Brillouin zone integrations were carried out using a Monkhorst–Pack k-point mesh [52] of $6 \times 8 \times 1$. For higher accuracy than possible with PBE, the electronic band structure was then calculated with the Heyd–Scuseria–Ernzerhof (HSE06) hybrid functional, with $nq_1 = nq_2 = nq_3 = 1$. Note that while theory places the Fermi level at the top of the valence band, the Fermi level in experiment is well within the band gap; thus, to compare theory with experiment, the binding energies from theory need to be offset by 0.34 eV.

III. SYMMETRIES OF THE OCCUPIED BANDS OF $HfSe_3$

The band structure of $HfSe_3(001)$ is highly anisotropic, as indicated by prior experimental [18] and theoretical band mappings [14]. The isokinetic energy contour plots near the top of the valence band, shown in Fig. 2, are illustrative of the anisotropic band structure of $HfSe_3(001)$. The binding energies chosen for the constant energy plots in Figs. 2(a) and 2(b) are based on the energies at which the bands are clearly visible. In Fig. 2(a) the incident x-ray polarization is along the chain direction (crystallographic $\vec{b}$ axis), and in Fig. 2(b), the incident light polarization is perpendicular to the chain direction, with these isoenergy plots taken at binding energies 0.3 and 0.5 eV below the top of the valence band, respectively. This indicates that the band structure is anisotropic. Furthermore, from Figs. 2(a) and 2(b) we can observe that the left and right sides of the constant energy plot are slightly different along $\bar{\Gamma}$ to $\bar{B}$. This lack of perfect mirror symmetry in the isoenergy plots is apparent at two different isoenergy cuts and for both even and odd symmetry. Although there is no mirror plane symmetry along $\bar{\Gamma}$ to $\bar{B}$ (with $\bar{\Gamma}$ to $\bar{Y}$ the nominal mirror plane), as is most evident in Fig. 2, there is also no mirror plane symmetry along the $\bar{\Gamma}$ to $\bar{Y}$ either (with $\bar{\Gamma}$ to $\bar{B}$ the nominal mirror plane). The lack of perfect mirror symmetry in the isoenergy plots is due to the lack of mirror plane inversion symmetry at the (001) crystal surface, so strictly speaking, the symmetry of the $HfSe_3(001)$ is lower than the nominal C_{2v} symmetry of a rectangle. As we look at the sample from the top, along the chains as in Fig. 1, we can see that the rectangular surface Brillouin zone is C_2 symmetric along $\vec{b}$ (y axis). We can also assign two vertical mirror planes, σ_{xz} and σ_{yz}, even though they are not true mirror planes due to the canted angle between the $\vec{a}$ and $\vec{c}$ axes and the general lack of inversion symmetry at the $HfSe_3(001)$ surface.

The DFT band-structure calculations provide a compelling picture that the contributions of Hf $-$ 5d orbitals and of the inner and outer Se $-$ 4p orbitals of the $HfSe_3(001)$ valence bands along $\bar{\Gamma}$ to $\bar{Y}$ and $\bar{\Gamma}$ to $\bar{B}$ high-symmetry directions can differ significantly, as shown in Figs. 3 and 4, respectively. The calculated spectral contributions from Hf $d_{3z^2-r^2}$ and selected additional rectangular representations, not shown in Figs. 3 and 4, are shown in the Supplemental Material (Figs. S3 and S4 [43]). As is fairly typical when comparing theory and experimental data for a semiconductor or insulator band structure, adding an offset to the Fermi level is needed to align theory with experiment. Along the $\bar{\Gamma}$ to $\bar{Y}$ direction of the surface Brillouin zone, the top of the valence band has dominant contributions from the inner Se p_y and Hf d_{xz} orbitals, followed by the contribution of the outer Se p_x orbital. There is a separation of the two bands at the top of the valence band, with spectral weight from Hf d_{xz} and significantly from the inner Se contributing to the band with a binding energy of 0.34 eV below the Fermi level, and that from the Hf $d_{x^2-y^2}$ and $d_{3z^2-r^2}$ and inner Se p_z and outer Se p_y orbitals contributing to the band 0.63 eV below the Fermi level at $\bar{\Gamma}$, as seen in Figs. 5 and 6. Among the Hf 5d orbitals, d_{xz} appears to be among the few that contribute to the top of the valence band, and it is strongly hybridized to the inner Se p_y. Although this Hf 5d_{xz} is an odd-symmetry band, contributions are allowed in the even geometry just the same, as there is no actual mirror plane along $\bar{\Gamma}$ to $\bar{Y}$ of the surface Brillouin zone (as discussed above). The strong valence-band contributions for the bands at greater binding energies, at around -1.09 eV, -1.33 eV (away from $\bar{\Gamma}$ point), -1.39 eV and -1.83 eV, are from the outer Se p_y, p_x, p_z and inner Se p_z orbitals, respectively. Among the Hf 5d orbitals, d_{xz}, d_{xy} and d_{zy} (d_{xy} and d_{zy} shown in Supplemental Material Fig. S3 [43]) provide contributions to the bands at binding energies of about -1.09 eV, -1.52 eV, and -1.39 eV, respectively, but these spectral weight contributions are smaller compared to the contributions from outer Se p_y, p_x, and p_z orbitals for the same greater-binding-energy valence bands.

The valence-band maximum along $\bar{\Gamma}$ to $\bar{B}$ direction (shown in Fig. 4), near the $\bar{\Gamma}$ point or the center of the Brillouin zone, has significant contributions from the inner Se p_y and Hf d_{xz} orbitals. Again, among the Hf 5d orbitals, d_{xz} is the only orbital that contributes to the top of the valence band. As seen in Fig. 5, as the wave vector increases away from the center ($\bar{\Gamma}$), the band increases in binding energy from around 0.34 eV below the Fermi level, and increased contributions from the outer Se p_y orbital all the way until the top valence band approaches closer to the Brillouin zone edge at $\bar{B}$, which is at around -0.9 eV. For the bands with binding energy farther from the Fermi level, at around -0.63 eV, -1.1 eV, -1.15 eV, and -1.39 eV, there are strong spectral contributions from the inner Se p_x and p_z; outer Se p_y; p_x and p_z orbitals,

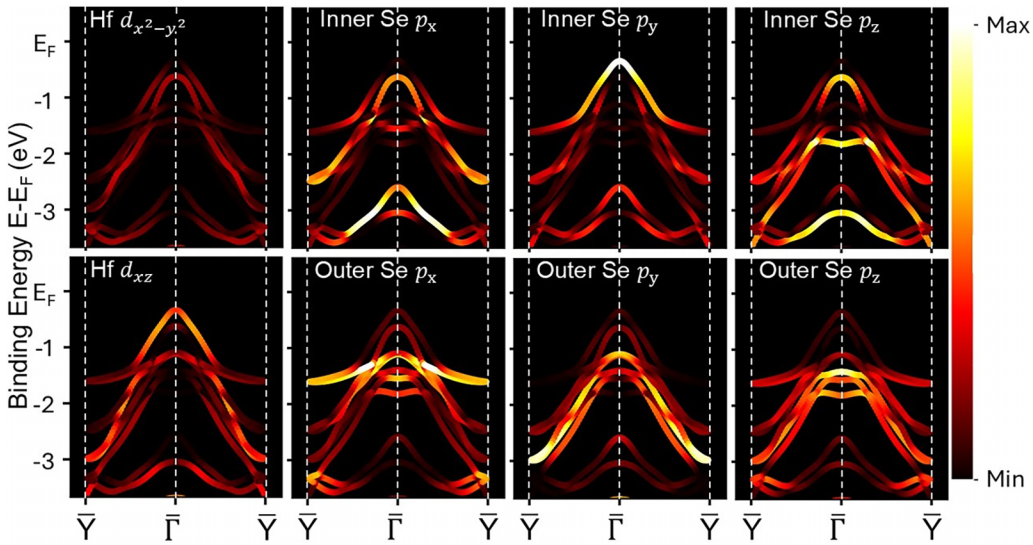

FIG. 3. A comparison of the orbital contribution of various bands to the valence-band structure of $HfSe_3(001)$ along $\bar{\mathbf{\Gamma}}$ to $\bar{\mathbf{Y}}$ high-symmetry direction of the surface Brillouin zone, based on DFT calculations. The brighter colors show more significant intensity from each orbital contribution. The inner and outer Se represents Se^{2-} and Se_2^{2-}, respectively. The Hf orbitals shown are the 5*d* orbitals and are labeled by their rectangular representation.

respectively. It is important to note that except for the inner Se p_y and p_x orbitals, all other orbital contributions are small, near the $\bar{\Gamma}$ point, the center of the Brillouin zone. Along $\bar{\Gamma}$ to $\bar{B}$ direction of the surface Brillouin zone, the Hf d_{xy} and d_{zy} orbitals contribute to the bands farther away from the Fermi level, well within the valence band, at binding energy around −1.1 eV, shown in Supplemental Material Fig. S4 [43].

Although the C_{2v} group symmetry, in Schönflies notation, is not strictly attributable to the $HfSe_3(001)$ surface Brillouin zone (because of the lack of mirror planes), there is value in applying photoemission symmetry selection rules [53,54] in the context of Fermi's golden rule using the C_{2v} point group, as shown in the case of $TiS_3(001)$ [4]. This is evident in the comparison of the calculated band structures for the $HfSe_3(001)$ orbitals and the corresponding experimental band structures as seen in Figs. 5, 6, and 7.

Not all the even-symmetry states, along $\bar{\Gamma}$ to $\bar{Y}$ direction of the surface Brillouin zone [Fig. 5(a)], dominate the experimental band structure measured by nano-ARPES in largely the *p*-polarization geometry [Fig. 5(b)]. The even-symmetry bands along $\bar{\Gamma}$ to $\bar{Y}$ include p_y, p_z, $d_{3z^2-r^2}$, $d_{x^2-y^2}$, and d_{yz}. The experimental band structure is, in fact, dominated by the Se p_y, Se p_z, $d_{3z^2-r^2}$, and Hf $d_{x^2-y^2}$ orbitals, with latter two orbitals clearly of a_1 irreducible representation. In spite of the fact that not all the orbitals of even symmetry contribute significantly to the experimental band structure at this photon

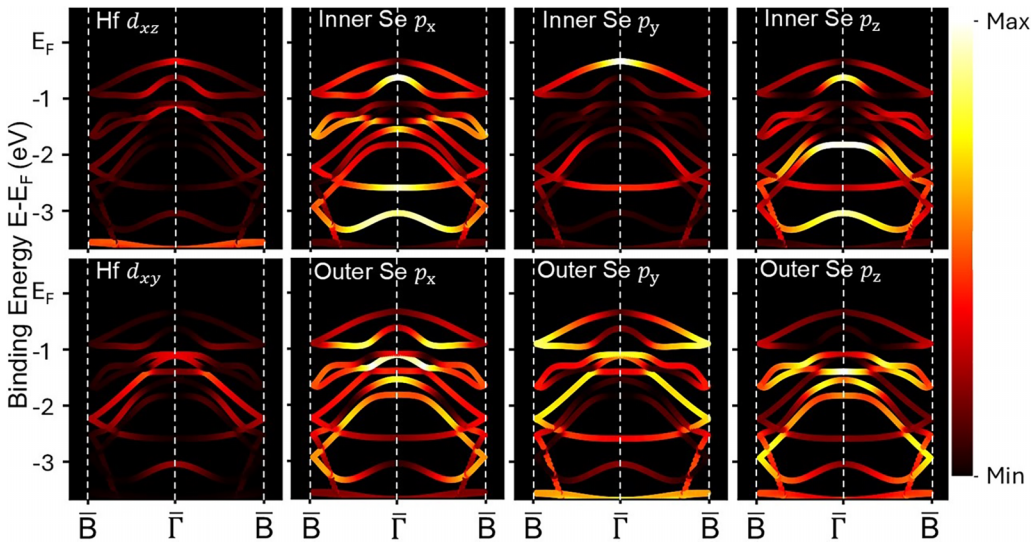

FIG. 4. A comparison of the orbital contribution of various bands to the valence-band structure of $HfSe_3(001)$ along $\bar{\mathbf{\Gamma}}$ to $\bar{\mathbf{B}}$ high-symmetry direction of the surface Brillouin zone, based on DFT. The brighter colors show more significant intensity from each orbital contribution. The inner and outer Se represents Se^{2-} and Se_2^{2-}, respectively.

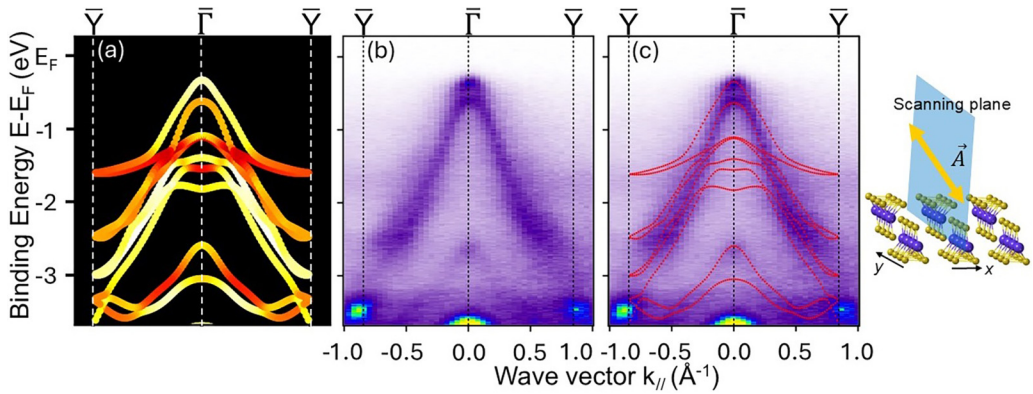

FIG. 5. (a) The even bands obtained from DFT calculations, with the valence-band maximum displaced by 0.34 eV, to greater binding energy to align with the experiment and (b) the experimental data from nano-ARPES, with the *p*-polarization geometry (i.e., with light vector potential largely along the scanning plane, as shown in the schematic), along $\bar{\mathbf{\Gamma}}$ to $\bar{\mathbf{Y}}$ direction of the surface Brillouin zone. The experimental band structure was obtained at a photon energy of 95 eV. (c) The superimposition of the DFT calculations on the experimental data. The critical point $\bar{\mathbf{Y}}$, at the surface Brillouin zone edge, occurs at 0.845 Å^{-1}.

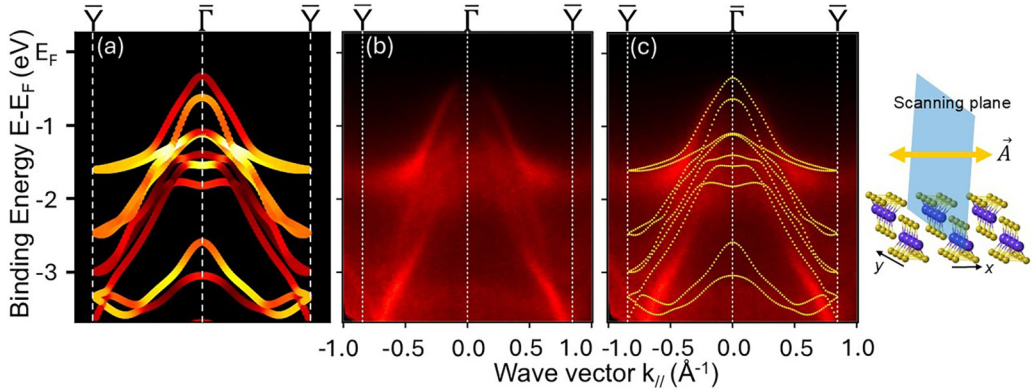

FIG. 6. (a) The odd bands obtained from DFT calculations, with the valence-band maximum displaced by 0.34 eV, to greater binding energy to align with the experiment and (b) the experimental data from nano-ARPES with *s*-polarization geometry (i.e., with incident light vector potential perpendicular to the scanning plane, as shown in the schematic) along $\bar{\mathbf{\Gamma}}$ to $\bar{\mathbf{Y}}$ direction of the surface Brillouin zone, taken at a photon energy of 95 eV. (c) The superimposition of the DFT calculations on the experimental data. The critical points at the surface Brillouin zone edges are at 0.845 Å^{-1}.

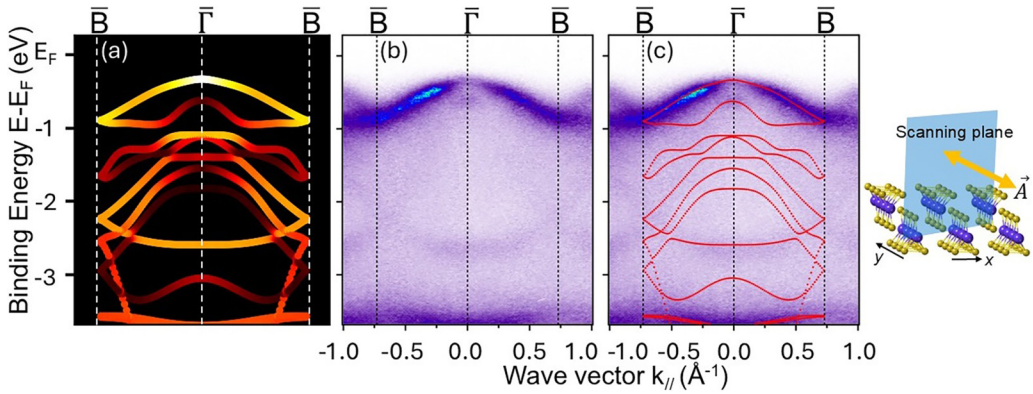

FIG. 7. (a) The odd bands obtained from DFT calculations, with the valence-band maximum displaced by 0.34 eV, to greater binding energy to align with the experiment and (b) the experimental data from ARPES with *s*-polarization geometry (i.e., with incident light vector potential perpendicular to the scanning plane, as shown in the schematic), in odd geometry, taken with 95-eV photon energy, both along $\bar{\mathbf{\Gamma}}$ to $\bar{\mathbf{B}}$ direction. (c) The superimposition of the DFT calculations on the experimental data. The critical points at the surface Brillouin zone edges are at 0.584 Å^{-1}.

energy, taken largely in the *p*-polarization geometry, experiment and theory show good agreement along $\bar{\Gamma}$ to $\bar{Y}$ direction of the surface Brillouin zone [Fig. 5(c)].

Now, on comparing our calculated band structure in the odd geometry along $\bar{\Gamma}$ to $\bar{Y}$ direction with the experimental data, we can see that the intensities at the top of the valence band are not prominent, as the top valence band near the $\bar{\Gamma}$ point is not evident in the nano-ARPES measurements, as shown in Fig. 6(b). The computed odd-symmetry bands [Fig. 6(a)] along $\bar{\Gamma}$ to $\bar{Y}$ arise from p_x and d_{xz}, but the experimental band structure obtained from angle-resolved photoemission in *s*-polarized geometry is dominated by the outer Se p_x and p_z orbitals and away from the center of the Brillouin zone ($\bar{\Gamma}$), and also by d_{xy}, rather significantly [Figs. 6(b) and 6(c)].

The even-symmetry bands along $\bar{\Gamma}$ to $\bar{B}$ should include the orbitals p_x, p_z, $d_{3z^2-r^2}$, $d_{x^2-y^2}$, and d_{xz}, while the odd-symmetry bands should have contributions from p_y and d_{yz}. The odd-symmetry bands along $\bar{\Gamma}$ to $\bar{B}$ in fact include the contributions from inner and outer Se $- p_y$ and Hf $- d_{yz}$ orbitals, as shown in Fig. 7(a), but the contributions from inner and outer Se are not equal, as the outer Se is at the surface. In fact, the experimental band structure contains significant contributions from the Se p_y orbital because of the odd geometry, while the outer Se p_y should dominate over the inner Se p_y orbital contribution. This explains the negligible experimental intensity at the top of the valence band at the center of the Brillouin zone ($\bar{\Gamma}$), along $\bar{\Gamma}$ to $\bar{B}$, with the intensity increasing with increasing wave vector away from the center of the Brillouin zone ($\bar{\Gamma}$). Thus, the weak photoemission intensity at the top of the valence band, for the center of the Brillouin zone ($\bar{\Gamma}$), in odd geometry, can be reconciled with theory [as shown in Fig. 7(c)] when one weights the outer Se orbital contributions which are stronger than the inner Se orbital contributions.

IV. THE ROLE OF SPIN-ORBIT COUPLING

As noted above, the nominal two vertical mirror planes, σ_{xz} and σ_{yz}, are not true mirror planes because of the canted angle between $\vec{a}$ and $\vec{c}$ axes and the general lack of inversion symmetry at the $HfSe_3(001)$ surface. This low inversion symmetry has already been noted for other trichalcogenides and leads to chiral effects and spin-orbit coupling, as seen for $TiS_3(001)$ [37]. The effect of spin-orbit coupling in lifting degeneracies is evident in Fig. 8(a) by comparing the splitting of some of the blue dotted curves (with the inclusion of spin-orbit interactions) to the red curves (no spin-orbit coupling) along Γ to A in the bulk-band-structure calculations. As shown in Fig. 5, there is a separation of the bands at the top of the valence band, seen in even geometry along $\bar{\Gamma}$ to $\bar{Y}$. The energy separation between the bands is estimated to be 0.22 ± 0.01 eV, as can be seen in Fig. 8(b). The energy separation of d_{xy} and $d_{x^2-y^2}$ ($m_l = -2$ and $m_l = 2$) at the top of the valence band is often a signature of spin-orbit splitting [42,55,56], but here, for the $HfSe_3(001)$ surface, there is a separation between bands of d_{xz} and $d_{x^2-y^2}$ ($m_l = 1$ and $m_l = 2$) symmetry, so not strictly speaking a spin-orbit splitting. This energy separation of the Hf 5*d* d_{xz} and $d_{x^2-y^2}$ bands at the top of the valence band, in the region of the center of the Brillouin zone ($\bar{\Gamma}$), is

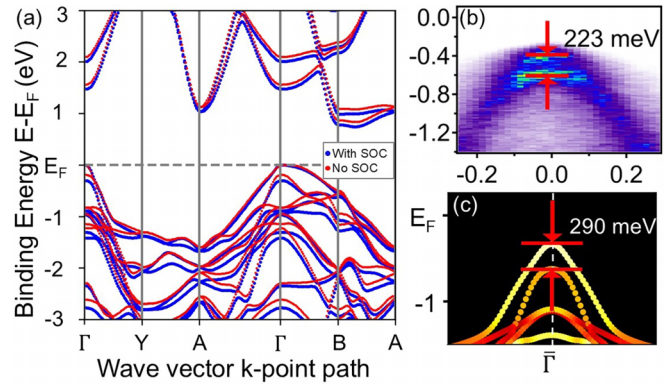

FIG. 8. (a) The DFT calculated band structure with spin-orbit coupling, shown in the blue dotted curve, unveils the splitting of bands along **Γ** to **Y** and **Y** to **A**. These splittings are not visible in the red dotted curves which were calculated without considering spin-orbit coupling. After the position of the valence-band maximum from theory has been shifted to align with experiment, the separation of the bands at the top valence band is highlighted in (b) and (c). The energy separation of these bands at the top of the valence band, seen in even geometry along $\bar{\mathbf{\Gamma}}$ to $\bar{\mathbf{Y}}$ direction in (b) experimental band structure, is 0.22 ± 0.01 eV, and from (c) DFT calculated band structure is 0.29 eV.

nonetheless sensitive to the intrinsic spin-orbit coupling, and this band separation increases in the presence of spin-orbit coupling. This is evident in the band-structure calculations of $HfSe_3$, with and without the inclusion of spin-orbit coupling, as shown in Fig. 8(a). We observe that the band separation at the top of the valence band increases along Γ to Y when spin-orbit coupling is included. The calculated effect of spin-orbit coupling is to increase the energy separation of the Hf 5*d* d_{xz} and $d_{x^2-y^2}$ bands, at the top of the valence band at the center of the surface Brillouin zone ($\bar{\Gamma}$), to -0.29 eV (E-E_F), as shown in Fig. 8(c). This is slightly larger than the experimentally measured energy separation 0.22 eV for the Hf 5*d* d_{xz} and $d_{x^2-y^2}$ bands, at the top of the valence band by 70 meV [Fig. 8(b)].

In fact, it is between the Y and A symmetry points of the Brillouin zone for the bulk band structure where the majority of the spin-orbit splitting occurs, as seen in the DFT calculations of Fig. 8(a). Thus, the band separation at the top of the valence band at the center of the Brillouin zone ($\bar{\Gamma}$) is not a true signature of spin-orbit splitting, in spite of previous suggestions otherwise [18]. Just the same, this energy separation between the $HfSe_3(001)$ bands of 220 meV, as can be seen in even geometry along $\bar{\Gamma}$ to $\bar{Y}$ [Fig. 8(b)], is much larger than the 110-meV band separation seen for $TiS_3(001)$ at the top of the valence band along $\bar{\Gamma}$ to $\bar{Y}$ [37].

V. THE EFFECTIVE HOLE MASSES AT THE TOP OF THE VALENCE BAND FOR THE OCCUPIED BANDS OF $HfSe_3(001)$

By comparing the experimental band structure along the $\bar{\Gamma}$ to $\bar{Y}$ and $\bar{\Gamma}$ to $\bar{B}$ directions of the $HfSe_3(001)$ surface Brillouin zone, specifically at the top of the valence band, the anisotropic nature of the bands along the orthogonal directions

TABLE I. A compilation of the effective hole mass of MX_3 (M = Ti, Zr, or Hf; X = S or Se) obtained from DFT calculations and experiments.

		$\bar{\Gamma}$ to $\bar{Y}$	$\bar{\Gamma}$ to $\bar{B}$
TiS_3	Theory	−0.98 [1,7]	−0.32 [1,7]
		−0.998 [8]	−0.308 [8]
		−0.99 [9]	−0.30 [9]
		−0.971 [10]	−0.321 [10]
		−0.83 [6]	−0.33 [6]
		Heavy [11]	Light [11]
		Heavy [12]	Light [12]
		Heavy [13]	Light [13]
	Experiment	−0.95 [2,3]	−0.37 [2,3]
ZrS_3	Theory	−0.682 [15]	−3.22 [15]
		−0.42 [7]	−1.28 [7]
		−0.321 [14]	−1.366 [14]
		−0.35 [10]	−1.703 [10]
		−0.31 [17]	−1.39 [17]
		Light [16]	Heavy [16]
	Experiment	−1.0 [18]	
		−0.87 [3]	−0.49 [3]
HfS_3	Theory	−0.313 [14]	−1.269 [14]
		−0.327 [10]	−1.356 [10]
$TiSe_3$	Theory	−0.85 [7]	−3.57 [7]
$ZrSe_3$	Theory	−0.161 [14]	−1.508 [14]
		−0.89 [7]	−2.36 [7]
		Light [16]	Heavy [16]
	Experiment	−0.7 [18]	
$HfSe_3$	Theory	−0.166 [14]	−0.862 [14]
		−0.25[a]	−1.11[a]
	Experiment	−0.8 [18]	
		−0.27[a]	−1.17[a]

[a]Represents the results obtained in this work.

of the surface Brillouin zone is clearly visible, which is not only clear from Fig. 2, but from comparing Figs. 5 and 7. The effective hole masses have been determined from the experimental band structure along both the $\bar{\Gamma}$ to $\bar{Y}$ and the $\bar{\Gamma}$ to $\bar{B}$ directions, using the parabolic fits, as indicated in the Supplemental Material (Fig. S5 [43]). The effective hole mass at the top of the valence bands along $\bar{\Gamma}$ to $\bar{Y}$ with even symmetry is $-0.27 \pm 0.01\,m_e$, whereas the effective hole mass along the direction perpendicular to the chains ($\bar{\Gamma}$ to $\bar{B}$) measured with s-polarization geometry is $-1.17 \pm 0.01\,m_e$. The effective hole mass along the direction perpendicular to the chains ($\bar{\Gamma}$ to $\bar{B}$) is clearly much higher than the effective hole mass along the chain direction (along $\bar{\Gamma}$ to $\bar{Y}$). These mass values align well with the hole effective mass determined through curve fitting of the band structure obtained from DFT calculations, which are $-0.25\,m_e$ along $\bar{\Gamma}$ to $\bar{Y}$ and $-1.11\,m_e$ along $\bar{\Gamma}$ to $\bar{B}$ (Supplemental Material Fig. S6 [43]).

The effective mass of the Hf $5d_{xz}$ and $d_{x^2-y^2}$ plus Se p_x band, observed just below the top of the valence band at $\bar{\Gamma}$ and also measured from the experimental band structure along the $\bar{\Gamma}$ to $\bar{Y}$ direction with odd symmetry, is $-0.43 \pm 0.01\,m_e$. This further establishes that the top of the valence band is evident in the p-polarization geometry but not in the s-polarization odd geometry, as observed in Figs. 5(b) and 6(b). From this work it is now clear that the top of the valence band was not identified in the prior work [18].

The effective hole mass along $\bar{\Gamma}$ to $\bar{B}$ direction determined from prior DFT calculated band structure of $-0.862\,m_e$ [14] is somewhat smaller (in terms of absolute values) than the measured value $-1.17\,m_e$ here and the current calculated value of $-1.11\,m_e$. The key point is that the light effective mass for $HfSe_3(001)$ is along $\bar{\Gamma}$ to $\bar{Y}$ not $\bar{\Gamma}$ to $\bar{B}$, as observed in the experimental band structure of $TiS_3(001)$ [2,3] and $ZrS_3(001)$ [3,18], as summarized in Table I.

The trichalcogenides are remarkable in that they are among the few crystalline systems for which the calculated band structure is not always a good predictor of experiment. Table I displays a comparison of the effective hole masses of different MX_3 (M = Ti, Zr, or Hf; X = S or Se) discussed here. Only a few systems, such as methyl ammonium bromide [57] and the trichalcogenides, as summarized in Table I, exhibit large variations in calculated effective hole masses. Such behavior is not only unusual because of the agreement between DFT and the measured occupied band structure is highly variable. For TiS_3, the calculated effective hole mass along $\bar{\Gamma}$ to $\bar{Y}$ and $\bar{\Gamma}$ to $\bar{B}$ is in the range $-0.83\,m_e$ [6] to $-0.99\,m_e$ [9] and $-0.3\,m_e$ [9] to $-0.33\,m_e$ [6], respectively, and resembles the experimentally measured values of $-0.95\,m_e$ [2] and $-0.37\,m_e$ [2] along $\bar{\Gamma}$ to $\bar{Y}$ and $\bar{\Gamma}$ to $\bar{B}$, respectively. For ZrS_3, the measured effective hole mass from $\bar{\Gamma}$ to $\bar{Y}$ is in the range of $-0.87\,m_e$ [3] to $-1.0\,m_e$ [18] and from $\bar{\Gamma}$ to $\bar{B}$ is $-0.49\,m_e$ [3], whereas the calculated effective hole mass is in the range of $-0.321\,m_e$ [17] to $-0.682\,m_e$ [15] from $\bar{\Gamma}$ to $\bar{Y}$ and is $-1.28\,m_e$ [7] to $-3.22\,m_e$ [15] from $\bar{\Gamma}$ to $\bar{B}$. Clearly, for ZrS_3, experiment and theory do not align. The experimental band-structure study on $ZrSe_3$ provided an effective hole mass of $-0.7\,m_e$ [18] along $\bar{\Gamma}$ to $\bar{Y}$, which is closer to the calculated value of $-0.89\,m_e$ [7] than the calculated value of -0.161 [14]. Obviously the estimates of the effective mass from theory vary widely for $ZrSe_3$, as is also the case for the calculated effective masses along $\bar{\Gamma}$ to $\bar{B}$, which is in the range of $-1.5\,m_e$ [14] to $-2.4\,m_e$ [7,14]. Here, the agreement between theory and experimental values for the effective hole masses seen for $HfSe_3(001)$ is quite good, and it is evident that the effective hole mass of $HfSe_3$ along the chains ($\bar{\Gamma}$ to $\bar{Y}$) is the lightest of all the reported values for other isostructural materials.

In all the above-discussed cases, summarized in Table I, strong in-plane anisotropy at the top valence bands is evident, emphasizing that for TMTs of the form MX_3, the electronic behavior can be different along different high-symmetry directions.

VI. CONCLUSION

We have studied the symmetry dependence of the band structure of quasi-one-dimensional $HfSe_3$ (001), along both high-symmetry directions, $\bar{\Gamma}$ to $\bar{Y}$ and $\bar{\Gamma}$ to $\bar{B}$, of the surface Brillouin zone using nano-ARPES measurements under p- and s-polarization geometry and DFT calculations. $HfSe_3$ (001) is a less studied member (compared to TiS_3 and ZrS_3) of a class of materials for which the understanding of the occupied band structure has been evolving over time. The experimental band structure measured with both geometries

along $\bar{\Gamma}$ to $\bar{Y}$ and $\bar{\Gamma}$ to $\bar{B}$ is shown here to align with the calculated band structure. The effective hole mass at the top of the valence band along $\bar{\Gamma}$ to $\bar{Y}$ is $-0.27 \pm 0.01\,m_e$, and $-1.17 \pm 0.01\,m_e$ along $\bar{\Gamma}$ to $\bar{B}$, determined from angle-resolved photoemission, similar to the calculated effective hole masses of $-0.25\,m_e$ and $-1.11\,m_e$ obtained from DFT along $\bar{\Gamma}$ to $\bar{Y}$ and $\bar{\Gamma}$ to $\bar{B}$, respectively, which is in exceptional agreement with the experimental measurements. We have identified that the effective hole mass of $HfSe_3$ along the chains ($\bar{\Gamma}$ to $\bar{Y}$) is the lightest of all the hole masses previously reported for the isostructural counterparts.

The band separation of 0.22 ± 0.01 eV of the bands at the top of the valence band along the $\bar{\Gamma}$ to $\bar{Y}$ direction of the $HfSe_3(001)$ surface Brillouin zone is not the result of spin-orbit splitting *per se*; this band separation, nonetheless, appears sensitive to spin-orbit coupling effects. This energy splitting is in good agreement with the value of 0.29 eV calculated from DFT.

ACKNOWLEDGMENTS

This research was supported by the National Science Foundation through Grant No. OIA-2521414 (P.A.D. and G.V.), the Future of Semiconductors "FuSe II" Grant No. 2425609 (P.A.D. and T.K.), Emergent Quantum Materials and Technologies (EQUATE) through Grants No. OIA-2044049 (G.V. and A.S.) and No. OSI-2329159 (A.L.), as well as support from the UNL Grand Challenges catalyst award "Quantum Approaches Addressing Global Threats." Additional financial support of Project TED2021-132656B-C21, granted under the 2021 Call "Ecological Transition and Digital Transition Projects," promoted by the Ministry of Science and Innovation, funded by the European Union through the "NextGenerationEU" program, the Recovery, Transformation, and Resilience Plan, and the State Research Agency (MCA) is also acknowledged. The DFT calculations were supported by the US Department of Energy under Grant No. DE-FG02-07ER46354 (B.A., D.L., and T.S.R.). Computational resources were provided by the UCF Advanced Research Computing Center.

DATA AVAILABILITY

The data that support the findings of this article are not publicly available upon publication because it is not technically feasible and/or the cost of preparing, depositing, and hosting the data would be prohibitive within the terms of this research project. The data are available from the authors upon reasonable request.

[1] J. Dai and X. C. Zeng, Titanium trisulfide monolayer: Theoretical prediction of a new direct-gap semiconductor with high and anisotropic carrier mobility, Angew. Chem. Int. Ed. **54**, 7572 (2015).

[2] H. Yi, T. Komesu, S. Gilbert, G. Hao, A. J. Yost, A. Lipatov, A. Sinitskii, J. Avila, C. Chen, M. C. Asensio, *et al.*, The band structure of the quasi-one-dimensional layered semiconductor $TiS_3(001)$, Appl. Phys. Lett. **112**, 052102 (2018).

[3] H. Yi, S. J. Gilbert, A. Lipatov, A. Sinitskii, J. Avila, J. Abourahma, T. Komesu, M. C. Asensio, and P. A. Dowben, The electronic band structure of quasi-one-dimensional van der Waals semiconductors: The effective hole mass of ZrS_3 compared to TiS_3, J. Phys.: Condens. Matter **32**, 29LT01 (2020).

[4] S. J. Gilbert, H. Yi, J.-S. Chen, A. J. Yost, A. Dhingra, J. Abourahma, A. Lipatov, J. Avila, T. Komesu, A. Sinitskii, *et al.*, Effect of band symmetry on photocurrent production in quasi-one-dimensional transition-metal trichalcogenides, ACS Appl. Mater. Interfaces **12**, 40525 (2020).

[5] M. Randle, A. Lipatov, A. Kumar, C.-P. Kwan, J. Nathawat, B. Barut, S. Yin, K. He, N. Arabchigavkani, R. Dixit, *et al.*, Gate-controlled metal–insulator transition in TiS_3 nanowire field-effect transistors, ACS Nano **13**, 803 (2019).

[6] J. A. Silva-Guillén, E. Canadell, P. Ordejón, F. Guinea, and R. Roldán, Anisotropic features in the electronic structure of the two-dimensional transition metal trichalcogenide TiS_3: Electron doping and plasmons, 2D Mater. **4**, 025085 (2017).

[7] Y. Jin, X. Li, and J. Yang, Single layer of MX_3 (M = Ti, Zr; X = S, Se, Te): A new platform for nano-electronics and optics, Phys. Chem. Chem. Phys. **17**, 18665 (2015).

[8] J. Kang, H. Sahin, H. D. Ozaydin, R. T. Senger, and F. M. Peeters, TiS_3 nanoribbons: Width-independent band gap and strain-tunable electronic properties, Phys. Rev. B **92**, 075413 (2015).

[9] Y. Aierken, D. Çakır, and F. M. Peeters, Strain enhancement of acoustic phonon limited mobility in monolayer TiS_3, Phys. Chem. Chem. Phys. **18**, 14434 (2016).

[10] A. Arora and A. De Sarkar, Advancing intrinsic carrier mobility estimation in transition metal trichalcogenide monolayers using DFT-BTE, Appl. Phys. Lett. **124**, 082101 (2024).

[11] J. Liu, Y. Guo, F. Q. Wang, and Q. Wang, TiS_3 sheet based van der Waals heterostructures with a tunable Schottky barrier, Nanoscale **10**, 807 (2018).

[12] R. Sun, Y. Gu, G. Yang, J. Wang, X. Fang, N. Lu, B. Hua, and X. Yan, Theoretical study on the interfacial properties of monolayer TiS_3–metal contacts for electronic device applications, J. Phys. Chem. C **123**, 7390 (2019).

[13] M. Arsentev, A. Missyul, A. V. Petrov, and M. Hammouri, TiS_3 magnesium battery material: Atomic-scale study of maximum capacity and structural behavior, J. Phys. Chem. C **121**, 15509 (2017).

[14] Q. Zhao, Y. Ren, L. Li, C. He, J. Che, R. Jia, Y. Xu, L. Zhu, and X. Xu, Flexibility and anisotropy of MX_3 (M = Zr, Hf; X = S, Se): New semiconductors with high photovoltaic performance, J. Appl. Phys. **134**, 124302 (2023).

[15] C. Wang, C. Zheng, and G. Gao, Bulk and monolayer ZrS_3 as promising anisotropic thermoelectric materials: A comparative study, J. Phys. Chem. C **124**, 6536 (2020).

[16] M. Li, J. Dai, and X. C. Zeng, Tuning the electronic properties of transition-metal trichalcogenides *via* tensile strain, Nanoscale **7**, 15385 (2015).

[17] R. Ahammed, A. Rawat, N. Jena, Dimple, M. K. Mohanta, and A. De Sarkar, ZrS_3/MS_2 and ZrS_3/MXY (M Mo, W; X, Y S, Se, Te; X ≠ Y) type-II van der Waals hetero-bilayers: Prospective candidates in 2D excitonic solar cells, Appl. Surf. Sci. **499**, 143894 (2020).

[18] D. Pacilé, M. Papagno, M. Lavagnini, H. Berger, L. Degiorgi, and M. Grioni, Photoemission and optical studies of $ZrSe_3$, $HfSe_3$, and ZrS_3, Phys. Rev. B **76**, 155406 (2007).

[19] X. Wang, T. Xiong, K. Xin, J. Yang, Y. Liu, Z. Zhao, J. Liu, and Z. Wei, Polarization sensitive photodetector based on quasi-1D $ZrSe_3$, J. Semicond. **43**, 102001 (2022).

[20] H. Li, G. Sanchez-Santolino, S. Puebla, R. Frisenda, A. M. Al-Enizi, A. Nafady, R. D'Agosta, and A. Castellanos-Gomez, Strongly anisotropic strain-tunability of excitons in exfoliated $ZrSe_3$, Adv. Mater. **34**, 2103571 (2022).

[21] A. Lipatov, J. Abourahma, G. Viswan, K. Acharya, T. R. Paudel, M. J. Loes, S. Bagheri, A. T. N'Diaye, E. Mishra, T. K. Ekanayaka, *et al.*, Electronic transport and polarization-dependent photoresponse in few-layered hafnium trisulfide (HfS_3) nanoribbons, J. Mater. Chem. C **11**, 9425 (2023).

[22] X. Wang, K. Wu, M. Blei, Y. Wang, L. Pan, K. Zhao, C. Shan, M. Lei, Y. Cui, B. Chen, *et al.*, Highly polarized photoelectrical response in vdW ZrS_3 nanoribbons, Adv. Electron. Mater. **5**, 1900419 (2019).

[23] A. Pant, E. Torun, B. Chen, S. Bhat, X. Fan, K. Wu, D. P. Wright, F. M. Peeters, E. Soignard, H. Sahin, *et al.*, Strong dichroic emission in the pseudo one dimensional material ZrS_3, Nanoscale **8**, 16259 (2016).

[24] S. Liu, W. Xiao, M. Zhong, L. Pan, X. Wang, H.-X. Deng, J. Liu, J. Li, and Z. Wei, Highly polarization sensitive photodetectors based on quasi-1D titanium trisulfide (TiS_3), Nanotechnology **29**, 184002 (2018).

[25] Z. Lian, Z. Jiang, T. Wang, M. Blei, Y. Qin, M. Washington, T.-M. Lu, S. Tongay, S. Zhang, and S.-F. Shi, Anisotropic band structure of TiS_3 nanoribbon revealed by polarized photocurrent spectroscopy, Appl. Phys. Lett. **117**, 073101 (2020).

[26] N. Papadopoulos, R. Frisenda, R. Biele, E. Flores, J. R. Ares, C. Sánchez, H. S. J. Van Der Zant, I. J. Ferrer, R. D'Agosta, and A. Castellanos-Gomez, Large birefringence and linear dichroism in TiS_3 nanosheets, Nanoscale **10**, 12424 (2018).

[27] A. Khatibi, R. H. Godiksen, S. B. Basuvalingam, D. Pellegrino, A. A. Bol, B. Shokri, and A. G. Curto, Anisotropic infrared light emission from quasi-1D layered TiS_3, 2D Mater. **7**, 015022 (2020).

[28] S. Hou, Z. Guo, J. Yang, Y. Liu, W. Shen, C. Hu, S. Liu, H. Gu, and Z. Wei, Birefringence and dichroism in quasi-1D transition metal trichalcogenides: Direct experimental investigation, Small **17**, 2100457 (2021).

[29] S. H. Suk, S. Nah, M. Sajjad, S. B. Seo, J. Song, N. Singh, and S. Sim, Polarization-driven ultrafast optical switching in TiS_3 nanoribbons via anisotropic hot carrier dynamics, Adv. Opt. Mater. **11**, 2300370 (2023).

[30] J. O. Island, R. Biele, M. Barawi, J. M. Clamagirand, J. R. Ares, C. Sánchez, H. S. J. Van Der Zant, I. J. Ferrer, R. D'Agosta, and A. Castellanos-Gomez, Titanium trisulfide (TiS_3): A 2D semiconductor with quasi-1D optical and electronic properties, Sci. Rep. **6**, 22214 (2016).

[31] S. Yang, M. Wu, W. Shen, L. Huang, S. Tongay, K. Wu, B. Wei, Y. Qin, Z. Wang, C. Jiang, *et al.*, Highly sensitive polarization photodetection using a pseudo-one-dimensional $Nb_{(1-x)}Ti_xS_3$ alloy, ACS Appl. Mater. Interfaces **11**, 3342 (2019).

[32] K. N. Boldyrev, E. V. Mostovshchikova, A. N. Titov, V. Ya. Pokrovskii, and I. G. Gorlova, Infrared transmission spectra of TiS_3: Fundamental absorption edge, phonons, and excitons, JETP Lett. **120**, 565 (2024).

[33] W. Kong, C. Bacaksiz, B. Chen, K. Wu, M. Blei, X. Fan, Y. Shen, H. Sahin, D. Wright, D. S. Narang, *et al.*, Angle resolved vibrational properties of anisotropic transition metal trichalcogenide nanosheets, Nanoscale **9**, 4175 (2017).

[34] S. Kurita, J. L. Staehli, M. Guzzi, and F. Lévy, Optical properties of ZrS_3 and $ZrSe_3$, Physica B+C **105**, 169 (1981).

[35] P. L. A. Ruano, D. Vaquero, E. Sánchez Viso, H. Li, F. Mompeán, F. Domínguez-Adame, A. Castellanos-Gomez, and J. Quereda, Polarization-sensitive photoresponse in few-layer $ZrSe_3$ photodetectors, 2D Mater. **12**, 015014 (2025).

[36] Z. Guo, H. Gu, M. Fang, B. Song, W. Wang, X. Chen, C. Zhang, H. Jiang, L. Wang, and S. Liu, Complete dielectric tensor and giant optical anisotropy in quasi-one-dimensional $ZrTe_5$, ACS Mater. Lett. **3**, 525 (2021).

[37] S. J. Gilbert, M. Li, J.-S. Chen, H. Yi, A. Lipatov, J. Avila, A. Sinitskii, M. C. Asensio, P. A. Dowben, and A. J. Yost, Chiral photocurrent in a quasi-1D TiS_3 (001) phototransistor, J. Phys.: Condens. Matter **35**, 124003 (2023).

[38] K. He, B. Barut, S. Yin, M. D. Randle, R. Dixit, N. Arabchigavkani, J. Nathawat, A. Mahmood, W. Echtenkamp, C. Binek, *et al.*, Graphene on chromia: A system for beyond-room-temperature spintronics, Adv. Mater. **34**, 2105023 (2022).

[39] P. A. Dowben, C. Binek, K. Zhang, L. Wang, W.-N. Mei, J. P. Bird, U. Singisetti, X. Hong, K. L. Wang, and D. Nikonov, Towards a strong spin–orbit coupling magnetoelectric transistor, IEEE J. Explor. Solid-State Comput. Devices Circuits **4**, 1 (2018).

[40] N. Sharma, J. P. Bird, C. Binek, P. A. Dowben, D. Nikonov, and A. Marshall, Evolving magneto-electric device technologies, Semicond. Sci. Technol. **35**, 073001 (2020).

[41] T. Komesu, D. Le, Q. Ma, E. F. Schwier, Y. Kojima, M. Zheng, H. Iwasawa, K. Shimada, M. Taniguchi, L. Bartels, *et al.*, Symmetry-resolved surface-derived electronic structure of MoS_2 (0001), J. Phys.: Condens. Matter **26**, 455501 (2014).

[42] I. Tanabe, T. Komesu, D. Le, T. B. Rawal, E. F. Schwier, M. Zheng, Y. Kojima, H. Iwasawa, K. Shimada, T. S. Rahman, *et al.*, The symmetry-resolved electronic structure of $2H-WSe_2$ (0 0 0 1), J. Phys.: Condens. Matter **28**, 345503 (2016).

[43] See Supplemental Material at http://link.aps.org/supplemental/10.1103/k4sz-qkh6 for the synthesis details of $HfSe_3$; images of the $HfSe_3$ nanowhiskers; room temperature x-ray diffraction spectra of the sample; additional comparison of the orbital contribution to the valence band along the chains and perpendicular to the chain directions; the fittings to the experimental band structure for the effective hole mass determinations; similar to the DFT calculated band structure for the theoretical effective hole mass calculations.

[44] S. Furuseth, L. Brattås, A. Kjekshus, A. F. Andresen, and P. Fischer, On the crystal structures of TiS_3, ZrS_3, $ZrSe_3$, $ZrTe_3$, HfS_3, and $HfSe_3$, Acta Chem. Scand. **29a**, 623 (1975).

[45] J. Avila, I. Razado-Colambo, S. Lorcy, B. Lagarde, J.-L. Giorgetta, F. Polack, and M. C. Asensio, ANTARES, a scanning photoemission microscopy beamline at SOLEIL, J. Phys.: Conf. Ser. **425**, 192023 (2013).

[46] J. Avila, I. Razado, S. Lorcy, R. Fleurier, E. Pichonat, D. Vignaud, X. Wallart, and M. C. Asensio, Exploring electronic structure of one-atom thick polycrystalline graphene films: A

nano angle resolved photoemission study, Sci. Rep. **3**, 2439 (2013).

[47] P. Giannozzi, S. Baroni, N. Bonini, M. Calandra, R. Car, C. Cavazzoni, D. Ceresoli, G. L. Chiarotti, M. Cococcioni, I. Dabo, *et al.*, QUANTUM ESPRESSO: A modular and open-source software project for quantum simulations of materials, J. Phys.: Condens. Matter **21**, 395502 (2009).

[48] J. P. Perdew, K. Burke, and M. Ernzerhof, Generalized gradient approximation made simple, Phys. Rev. Lett. **77**, 3865 (1996).

[49] J. P. Perdew, J. A. Chevary, S. H. Vosko, K. A. Jackson, M. R. Pederson, D. J. Singh, and C. Fiolhais, Atoms, molecules, solids, and surfaces: Applications of the generalized gradient approximation for exchange and correlation, Phys. Rev. B **46**, 6671 (1992).

[50] S. Grimme, Accurate description of van der Waals complexes by density functional theory including empirical corrections, J. Comput. Chem. **25**, 1463 (2004).

[51] D. R. Hamann, Optimized norm-conserving Vanderbilt pseudopotentials, Phys. Rev. B **88**, 085117 (2013).

[52] H. J. Monkhorst and J. D. Pack, Special points for Brillouin-zone integrations, Phys. Rev. B **13**, 5188 (1976).

[53] H.-P. Steinrück, Angle-resolved UV-photoelectron spectroscopy, Vacuum **45**, 715 (1994).

[54] M. Tinkham, *Group Theory and Quantum Mechanics* (McGraw-Hill, New York, 1964).

[55] D. Le, A. Barinov, E. Preciado, M. Isarraraz, I. Tanabe, T. Komesu, C. Troha, L. Bartels, T. S. Rahman, and P. A. Dowben, Spin–orbit coupling in the band structure of monolayer WSe_2, J. Phys.: Condens. Matter **27**, 182201 (2015).

[56] I. Tanabe, M. Gomez, W. C. Coley, D. Le, E. M. Echeverria, G. Stecklein, V. Kandyba, S. K. Balijepalli, V. Klee, A. E. Nguyen, *et al.*, Band structure characterization of WS_2 grown by chemical vapor deposition, Appl. Phys. Lett. **108**, 252103 (2016).

[57] T. Komesu, X. Huang, T. R. Paudel, Y. B. Losovyj, X. Zhang, E. F. Schwier, Y. Kojima, M. Zheng, H. Iwasawa, K. Shimada, *et al.*, Surface electronic structure of hybrid organo lead bromide perovskite single crystals, J. Phys. Chem. C **120**, 21710 (2016).